



Cooperatively tailored surface frustrated Lewis pairs and N-doping on CeO₂ for photocatalytic CO₂ reduction to high-value hydrocarbon products

Xinying Yan^{a,1}, Bo Gao^{a,1}, Xiaoli Zheng^{a,*}, Mingjie Cheng^a, Nan Zhou^a, Xueqi Liu^b, Lina Du^c, Fei Yuan^d, Jing Wang^a, Xiaomin Cui^a, Gaoxiang Zhang^a, Weiqian Kong^a, Qun Xu^{a,b,**}

^a Department of Materials Science and Engineering, Zhengzhou University, Zhengzhou 450001, PR China

^b Henan Institute of Advanced Technology, Zhengzhou University, Zhengzhou 450003, PR China

^c Henan Key Laboratory of Nanocomposites and Applications Institute of Nanostructured Functional Materials, Huanghe Science and Technology College, Zhengzhou 450006, PR China

^d School of Chemistry and Chemical Engineering, Henan University of Science and Technology, Luoyang, Henan, 471000, PR China

ARTICLE INFO

Keywords:

CO₂ photocatalytic reduction
Cerium oxide
Frustrated Lewis Pairs
N-doping
C-C coupling

ABSTRACT

Photocatalytic conversion of CO₂ into high valuable fuels has attracted great interest, especially for the multi-carbon products. We design and synthesize a cerium oxide (CeO₂) photocatalyst with cooperatively tailored N-doping and surface frustrated Lewis pairs (FLPs), wherein the FLPs are constructed by Lewis acidic coordinatively unsaturated Ce³⁺ species and the adjacent Lewis basic Ce-OH groups. The synergistic effects of the FLPs and N-doping cooperatively promote the light absorption, CO₂ bonding and activation, multiple proton-electron transfer processes and C-C coupling reactions, thereby improving the productivity and selectivity of photoreduction of CO₂ to high-value hydrocarbons. The finely surface engineered CeO₂ photocatalysts achieve 86.86% selectivity of C₁ (CO, CH₄) and C₂ (C₂H₄ and C₂H₂) hydrocarbon products, and the selectivity for the C₂ products reaches to 41.07%. It proves that the ceria catalyst is promising toward practical production of high-value multicarbon fuels using solar energy.

1. Introduction

Photocatalytic conversion of CO₂ into valuable hydrocarbons realizes solar-to-chemical energy conversion, which is a desirable strategy to kill two birds with one stone, that is, CO₂ photoreduction can not only tackle energy shortage but also keep global carbon balance. At the moment, one carbon (C₁) products such as carbon monoxide (CO), methane (CH₄), formate (HCOOH) or methanol (CH₃OH) are generally the major products of photocatalytic CO₂ reduction [1–6]. Chemical products with two or more carbons (C₂ or C₂₊) are much more attractive compared to the C₁ ones due to their higher energy content and market price [7]. Particularly, C₂ hydrocarbons such as ethylene (C₂H₄) and ethyne (C₂H₂) have high demands in the chemical industry, which are highly important chemical raw materials. Nevertheless, the regulation of multiple proton-electron transfer processes and C-C coupling reactions for the production of high value-added C₂H₄ and C₂H₂ chemicals are full of challenge, especially for the C₂H₂ [8]. Recently, many

strategies have been developed to drive the product selectivity of photocatalytic CO₂ reduction toward C₂ or C₂₊ hydrocarbons, including heterostructure construction [9,10], doping [11], alloying [12] and defect engineering [13]. Wang et al. reported that the active sites of Cu and Ce in a Cu^{δ+}/CeO₂-TiO₂ photocatalyst can cooperatively facilitate the adsorption and activation of CO₂, stabilize the *CO intermediates, promote C-C coupling, and thus improve the efficiency and selectivity of photocatalytic CO₂ reduction to C₂H₄ [9]. Gao et al. demonstrated that introduction of sulfur vacancy in AgInP₂S₆ could cause the charge accumulation on the nearby Ag atoms, which can effectively trap *CO and reduce the potential barrier of C-C coupling to C₂ products [13]. However, at the moment, it is still challenging to simultaneously increase the productivity of photocatalytic CO₂ reduction and promote the selectivity of C₂ products through surface engineering.

Frustrated Lewis pairs (FLPs), sterically encumbered Lewis acid/base combinations, have been anticipated as a promising surface engineering strategy to activate many small molecules (e.g. H₂, NO and CO₂) and

* Corresponding author.

** Corresponding author at: Department of Materials Science and Engineering, Zhengzhou University, Zhengzhou 450001, PR China.

E-mail addresses: xzhengab@zhu.edu.cn (X. Zheng), qunxu@zhu.edu.cn (Q. Xu).

¹ X. Yan and B. Gao contributed equally to this work.

induce electron transfer [14–16]. Recently, heterogeneous catalysts with FLPs have been well developed to efficiently photocatalytic reduction of CO₂, wherein the bonding and antibonding orbitals of CO₂ could interact with and induce electron transfer with the FLPs, producing a synergetic activation effect [17–20]. Ozin et al. reported that the FLPs created by a Lewis acidic coordinately unsaturated surface indium site proximal to an oxygen vacancy and a Lewis basic surface hydroxide site in In₂O_{3-x}(OH)_y and Bi-substituted one enable heterogeneous photocatalytic CO₂ reduction to CO and CH₄ [21–25]. Moreover, many bimetallic oxyhydroxide/oxides/hydroxides photocatalysts with surface FLPs, such as CoGeO_{2-x}(OH)_y [17], Bi_xIn_{1-x}O₃ [26], ZnSn(OH)₆ [27] can also efficiently capture, activate, and reduce CO₂. In these cases, the oxygen vacancies and hydroxides has been well established to be able to construct the FLPs and accelerate the photocatalytic reduction of CO₂. Nevertheless, the major products of photocatalytic CO₂ reduction based on the FLPs are typically CO and CH₄. How to tailor the reactivity of the FLPs for C₂ products is rarely mentioned.

Nanostructured cerium oxide (CeO₂) has been widely regarded as one of the typical heterogeneous catalysts in that a high proportion of oxygen vacancies and coordination unsaturated Ce³⁺ species existed in CeO₂ could act as efficient active sites for catalysis [28–30]. The FLPs constructed on the defect-enriched CeO₂ (reduced Ce³⁺ atoms near an oxygen vacancy as Lewis acids and the adjacent surface lattice O as the Lewis base) have been reported for hydrogenation of alkenes and alkynes as well as activation and cyclization of CO₂ [31,32]. According to the above studies, it can be observed that CeO₂ holds great potential in photocatalytic reduction of CO₂ into valuable chemicals [33,34]. However, few reports have shown that C₂ products can be efficiently generated using CeO₂ as a single catalyst. The main reason might be that the geometry and electronic state of the active site on CeO₂ are not conducive to the C-C coupling for the formation of C₂ products. Therefore, the development of suitable active sites on CeO₂ photocatalysts through surface engineering might be an important way to promote the production of high-value C₂ hydrocarbons.

In this work, surface FLPs and N-doping are cooperatively tailored on the CeO₂ with the addition of ammonium hydroxide (NH₃·H₂O). Herein, NH₃·H₂O acts as a base source, providing abundant unsaturated Ce³⁺ sites and -OH groups as well as N-doping for finely engineering the surface of the CeO₂. The surface FLPs on the CeO₂ were constructed by Lewis acidic coordinately unsaturated Ce³⁺ species and the adjacent Lewis basic Ce-OH groups. The N-doping can not only induce the reduction of Ce⁴⁺ to Ce³⁺ and further increase the Lewis acidity, also be able for bandgap narrowing for efficient light harvesting and charge transfer. The synergistic effects of the FLPs and N-doping cooperatively contribute to the effective photocatalytic reduction of CO₂ to CO and CH₄ with high productivity as well the deeper activation of CO₂, further improve the activity of the entire tandem reaction to C₂ (C₂H₄ and C₂H₂) hydrocarbon products.

2. Experimental section

2.1. Materials

Cerous nitrate hexahydrate (Ce(NO₃)₃·6 H₂O, 99.95%, Shanghai Macklin Biochemical Co., Ltd), ammonium hydroxide (NH₃·H₂O, 28%, Luoyang Haohua Chemical reagent Co., Ltd), sodium hydroxide (NaOH, 96%, Sinopharm Chemical Reagent Co., Ltd), triethanolamine (TEOA, 99%, Sinopharm Chemical Reagent Co., Ltd), pyrrole (C₄H₅N, 99%, Shanghai Aladdin Biochemical Technology Co., Ltd.), pyridine (C₅H₅N, 99.5%, Sinopharm Chemical Reagent Co., Ltd) and absolute ethanol (99.7%, Tianjin Fuyu Fine Chemical Co., Ltd) were purchased. Water used in the experiments was deionized water. All the chemicals were used as purchased without purification.

2.2. Synthesis of CeO₂-AH and CeO₂-AH-C

In the typical synthesis, 2.5 g of cerous nitrate hexahydrate (Ce(NO₃)₃·6 H₂O) was added into 62 mL of deionized water to form the solution, the 8 mL aqueous ammonium hydroxide (NH₃·H₂O) was added to this solution gradually. After vigorous stirring at room temperature for 30 min, the suspension was transferred into a Teflon-lined autoclave (100 mL) and heated at 90 °C for 6 h. After cooling to room temperature, the product was washed twice with deionized water and ethanol alternately to remove the impurity ion from the solution, then dried under vacuum in freeze dryer. For convenience, the sample prepared by the ammonium hydroxide was denoted as CeO₂-AH. For comparison, the above obtained CeO₂-AH was further calcined at 500 °C for 4 h in air and the calcinated CeO₂-AH was named as CeO₂-AH-C.

2.3. Characterization

The crystal structure was determined by Philips type PW1825 X-ray diffractometer with CuKα light source radiation. The morphology of the catalyst was observed by scanning electron microscopy (SEM, JEOL 6700 F), transmission electron microscopy (TEM, JEOL 2010 F) and high resolution transmission electron microscopy. X-ray photoelectron spectroscopic (XPS) analysis was performed using a PHI5600 XPS spectrometer, and all binding energies were calibrated with reference to standard carbon C 1 s = 284.6 eV. Fluorescence spectrometer (F-7000) was used to record the photoluminescence (PL) and time-resolved fluorescence spectra at room temperature. The excitation wavelength was 400 nm and the starting wavelength was 420 nm. Shimadzu UV-3010 spectroscopy was used to determine the ultraviolet-visible diffuse reflectance spectrum (UV-Vis DRS) of the materials. Barium sulfate was selected as the reference here. The FT-IR spectra (Nicolet 5700) were collected from 400 to 3000 cm⁻¹ at a spectral resolution of 4 cm⁻¹ on the spectrometer. Raman spectra were determined on a LABRAM-HR confocal laser with He-Cd lasers at a 532 nm excitation source. The electron paramagnetic resonance (EPR) measurements were performed using a Bruker EMX-9.5/12 system. CO₂ programmed temperature desorption (CO₂-TPD) was measured in the reaction tube with 75 mg catalyst, and the temperature was programmed from room temperature to 300 °C at the rate of 10 °C/min for drying pretreatment. After pretreatment, He atmosphere flow (30 mL/min) was purged for 1 h, after cooling to 50 °C, 10% CO₂/He mixture (30 mL/min) was purged for 1 h until saturation. Switching He atmosphere flow (30 mL/min) to purge for 1 h to remove weak physical adsorption on the surface, and finally desorption at a temperature rate of 10 °C/min at 600 °C in He atmosphere.

Photocurrent response and electrochemical impedance spectroscopy (EIS) tests were detected by an electrochemical workstation (CHI 660D) with a standard three electrochemical system. 3 mg of catalyst was dispersed in a mixture of 0.5 mL deionized water and 0.1 mL anhydrous ethanol and then dripped onto FTO glass (1 × 1 cm²). The working electrode was placed to air for 5 h to remove ionized water and ethanol. 1 × 1 cm² FTO with catalyst, Ag/AgCl and platinum wire were used as working electrode (WE), reference electrode (RE) and counter electrode (CE), respectively. The electrolyte is 0.5 M Na₂SO₄ solution, and the lighting source is 300 W xenon lamp to provide simulation of sunlight.

2.4. Photocatalytic reduction of CO₂

Photocatalytic reduction of CO₂ was carried out in a 100 mL of transparent closed quartz reaction cell with a quartz window, placed on a magnetic stirrer. First, 36 mL of deionized water, 4 mL of TEOA, and 1 mg of catalyst were added to the reactor. After mixing with stirring and ultrasound, CO₂ (99.99%) at approximately was introduced through a

flow meter for 30 min (The flow rate of carbon dioxide was 7 mL/min). The above cleaning process to remove as much air from the reaction system as possible. The condensate is channeled into the outer wall of the reactor, and the temperature of the entire reaction system was kept stable at 25 °C. Under light irradiation (a 300 W Xeon lamp was used as the light source, the optical power density is 500 mW/cm²), the gas products were passed into a gas chromatograph (GC) for detection. Carbon-containing products such as carbon monoxide (CO), methane (CH₄), ethylene (C₂H₄), ethane (C₂H₆) and acetylene (C₂H₂) were calibrated and analyzed by flame ionization detector (FID), hydrogen and

other gases that do not contain carbon were calibrated and detected by thermal conductivity detector (TCD). The ¹³CO₂ isotope labeling reaction was collected in a photoreduction reactor in the presence of CeO₂-AH catalyst, and the ¹³CO₂ isotope products were analyzed by Hiden Analytical (HPR-40) differential electrochemical mass spectrometer.

The calculation formula for the selectivity of the carbon product is as following:

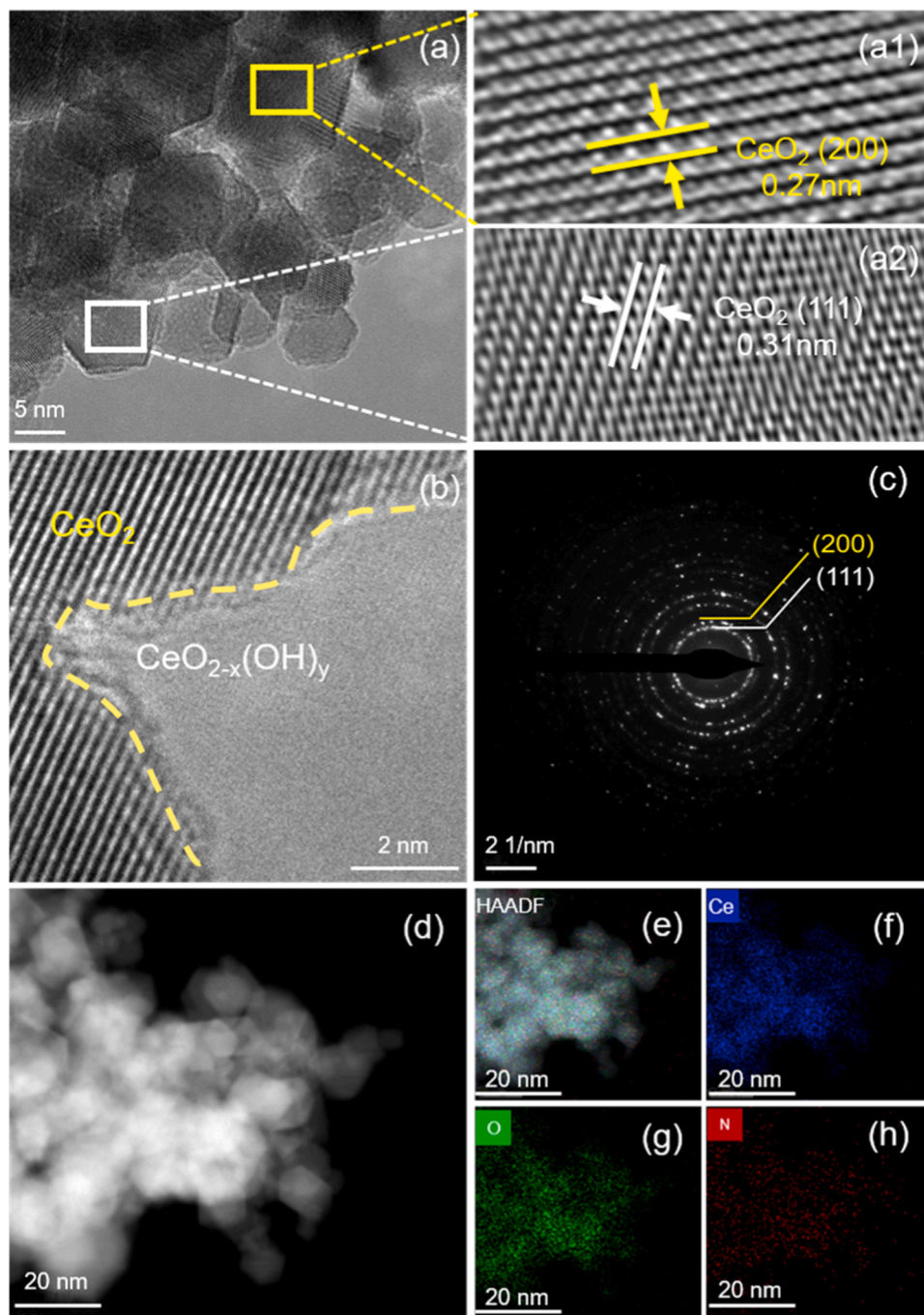


Fig. 1. Morphology characterization of the CeO₂-AH catalyst. (a) TEM image of CeO₂-AH, (a1, a2) Bragg filtered images of the lattice fringe reflection enclosed by square box in (a). (b) HRTEM image of CeO₂-AH. (c) SAED pattern of CeO₂-AH. (d-h) EDX element mapping images of CeO₂-AH.

$$\text{Selectivity}(\chi) = \frac{\text{Yield}_{(\chi)} \times Y_{e^{-}}}{\text{Yield}_{(\text{H}_2)} \times 2e^{-} + \text{Yield}_{(\text{CO})} \times 2e^{-} + \text{Yield}_{(\text{CH}_4)} \times 8e^{-} + \text{Yield}_{(\text{C}_2\text{H}_4)} \times 12e^{-} + \text{Yield}_{(\text{C}_2\text{H}_2)} \times 10e^{-}}$$

wherein the *Yield* is denoted as the product yield ($\mu\text{mol g}^{-1} \text{h}^{-1}$), and the *Y* represents the number of electrons required for the reduction of CO_2 to the related carbon products, *Y* is 2, 2, 8, 12 and 10 for H_2 , CO, CH_4 , C_2H_4 and C_2H_2 , respectively.

2.5. DFT computational methods

Density functional theory (DFT) calculations were performed with a Vienna Ab-initio Simulation Package (VASP) code [35] utilizing the projector augmented wave method (PAW) [36]. The exchange-correlation energy was described by the Perdew-Burke-Ernzerhof (PBE) under the generalized gradient approximation (GGA) [37]. A vacuum space of 10 Å was set to avoid the interaction between periodical images. The kinetic cut-off energy was set to 500 eV for the plane wave base set. The Monkhorst-Pack method [38] was used for sampling the Brillouin zone k-point mesh of $(4 \times 4 \times 1)$. Electron self-consistent relaxation and ion relaxation adopt convergence criteria, with convergence threshold of 10^{-4} eV for total electronic energy and 0.02 eV/Å for remaining total force.

The Gibbs free energy change (ΔG) for each step of the photocatalytic CO_2 reduction was calculated as follows:

$$\Delta G = \Delta E + \Delta \text{ZPE} - T\Delta S \quad (T = 298.15 \text{ K})$$

where ΔE , ΔZPE , and ΔS represent the change of reaction energy, zero-point energy and entropy, respectively.

The zero-point energy and entropy correction were obtained from the NIST-JANAF thermodynamics table for gas molecules, and by calculating the vibration frequency of the intermediate adsorbent, respectively.

3. Results and Discussion

3.1. Structure characterization of the $\text{CeO}_2\text{-AH}$ catalyst

The $\text{CeO}_2\text{-AH}$ was prepared by a simple hydrothermal approach with the assistance of $\text{NH}_3\text{-H}_2\text{O}$. For comparison, the $\text{CeO}_2\text{-AH}$ calcinated in air ($\text{CeO}_2\text{-AH-C}$) was also prepared. The morphology of the samples was first explored by scanning electron microscopy (SEM) and transmission

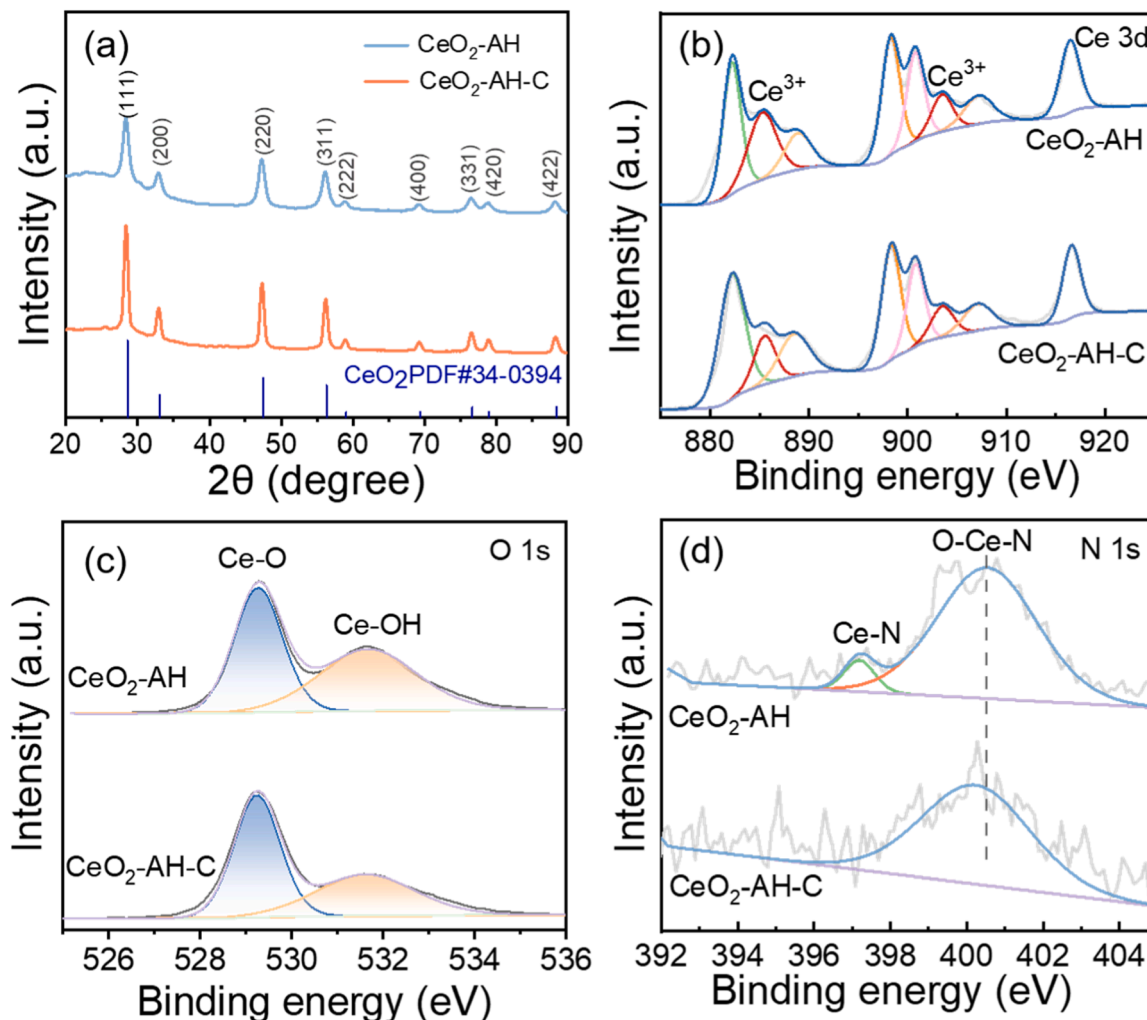


Fig. 2. (a) XRD patterns of $\text{CeO}_2\text{-AH}$ and $\text{CeO}_2\text{-AH-C}$. High-resolution (b) Ce 3d, (c) O 1s and (d) N 1s XPS spectra of $\text{CeO}_2\text{-AH}$ and $\text{CeO}_2\text{-AH-C}$.

electron microscopy (TEM). The $\text{CeO}_2\text{-AH}$ exhibit nanoparticle morphology with the size about 19 nm (Fig. 1a and Fig. S1a). After calcination, the $\text{CeO}_2\text{-AH-C}$ show the similar morphology as that of $\text{CeO}_2\text{-AH}$ (Fig. S1b). As shown in Fig. 1a, the $\text{CeO}_2\text{-AH}$ exhibit good crystallinity and the Bragg filtered images of the lattice fringe reflection enclosed by square box in Fig. 1a display the lattice spacing of 0.27 nm and 0.31 nm, corresponding to (200) and (111) crystal plane of CeO_2 , respectively. Notably, the high-resolution TEM image of the $\text{CeO}_2\text{-AH}$ in Fig. 1b show that a 0.50–2.00 nm-thick amorphous shell is coated outside the crystalline CeO_2 . The selected-area electron diffraction (SAED) pattern of the $\text{CeO}_2\text{-AH}$ (Fig. 1c) is in accordance with the (200) and (111) crystalline planes of CeO_2 . The presence of diffraction spots and rings together in the SAED pattern suggest that the $\text{CeO}_2\text{-AH}$ possess crystalline and amorphous regions, which is consistent with the TEM results. The energy dispersive X-ray (EDX) elemental mapping images in Fig. 1d-h reveal the homogeneous distribution of Ce, O and N elements on the $\text{CeO}_2\text{-AH}$, confirming that the N element are well incorporated in the $\text{CeO}_2\text{-AH}$. From the integrated EDX spectrum, a total atomic content of N is 5.85% for $\text{CeO}_2\text{-AH}$.

The crystal structures of the samples were analyzed by X-ray diffraction (XRD). The XRD pattern of the $\text{CeO}_2\text{-AH}$ is consistent with the face-centered cubic structure of CeO_2 (PDF# 34-0394), and no other phases are present (Fig. 2a). These nine peaks centered at 2θ of 28.55° , 33.08° , 47.47° , 56.33° , 59.09° , 69.40° , 76.70° , 79.07° and 88.41° are well assigned to the (111), (200), (220), (311), (222), (400), (331), (420) and (422) planes of CeO_2 , respectively. The d-spacings are determined to be 0.31 and 0.27 nm for the (111) and (200) plane of

$\text{CeO}_2\text{-AH}$, respectively, which are well harmonized with that computed by HRTEM. The $\text{CeO}_2\text{-AH-C}$ exhibit the similar XRD pattern as that of $\text{CeO}_2\text{-AH}$ but with increased crystallinity, indicating that the calcination might partially remove the amorphous shell.

XPS measurements were carried out to analyze the chemical structure and atomic valence state of the samples. To obtain more details on the nature of the coordination between atoms, high-resolution Ce 3d, O 1s, and N 1s XPS spectra were carried out. As shown in Fig. 2b, the two peaks at 885.28 eV and 903.48 eV are ascribed to Ce^{3+} and the other six peaks correspond to Ce^{4+} species. As listed in Table S1, the $\text{CeO}_2\text{-AH}$ exhibits a higher concentration of Ce^{3+} species (27.1%) as compared to the $\text{CeO}_2\text{-AH-C}$ (14.5%). Considering that oxygen vacancies can be generated to keep charge balance due to the reduction of Ce^{4+} to Ce^{3+} , the high concentration of coordinately unsaturated Ce^{3+} ions nearby the oxygen vacancy in $\text{CeO}_2\text{-AH}$ can provide abundant Lewis acid sites. Fig. 2c present the high-resolution O 1s XPS spectra of $\text{CeO}_2\text{-AH}$ and $\text{CeO}_2\text{-AH-C}$. The peaks at 529.27 eV and 531.66 eV are corresponded to lattice oxygen (Ce-O) and Ce-OH, respectively [39]. Noteworthy, the peak area ratio of Ce-OH in $\text{CeO}_2\text{-AH}$ (49.7%) is higher compared with $\text{CeO}_2\text{-AH-C}$ (41.8%), showing that more Ce-OH groups are present on the $\text{CeO}_2\text{-AH}$ than that of $\text{CeO}_2\text{-AH-C}$, which can act as the Lewis base sites. The N 1s XPS profile of the $\text{CeO}_2\text{-AH}$ (Fig. 2d) is deconvoluted into two main peaks centered at binding energies of 397.18 and 400.48 eV, which are allocated as Ce-N bond and O-Ce-N, respectively [40–42]. This result suggests that N atoms substitute for the O in the $\text{CeO}_2\text{-AH}$ and signify the formation of Ce-N and O-Ce-N structure. Likewise, the N 1s peaks in the $\text{CeO}_2\text{-AH-C}$ are significantly decreased compared with that

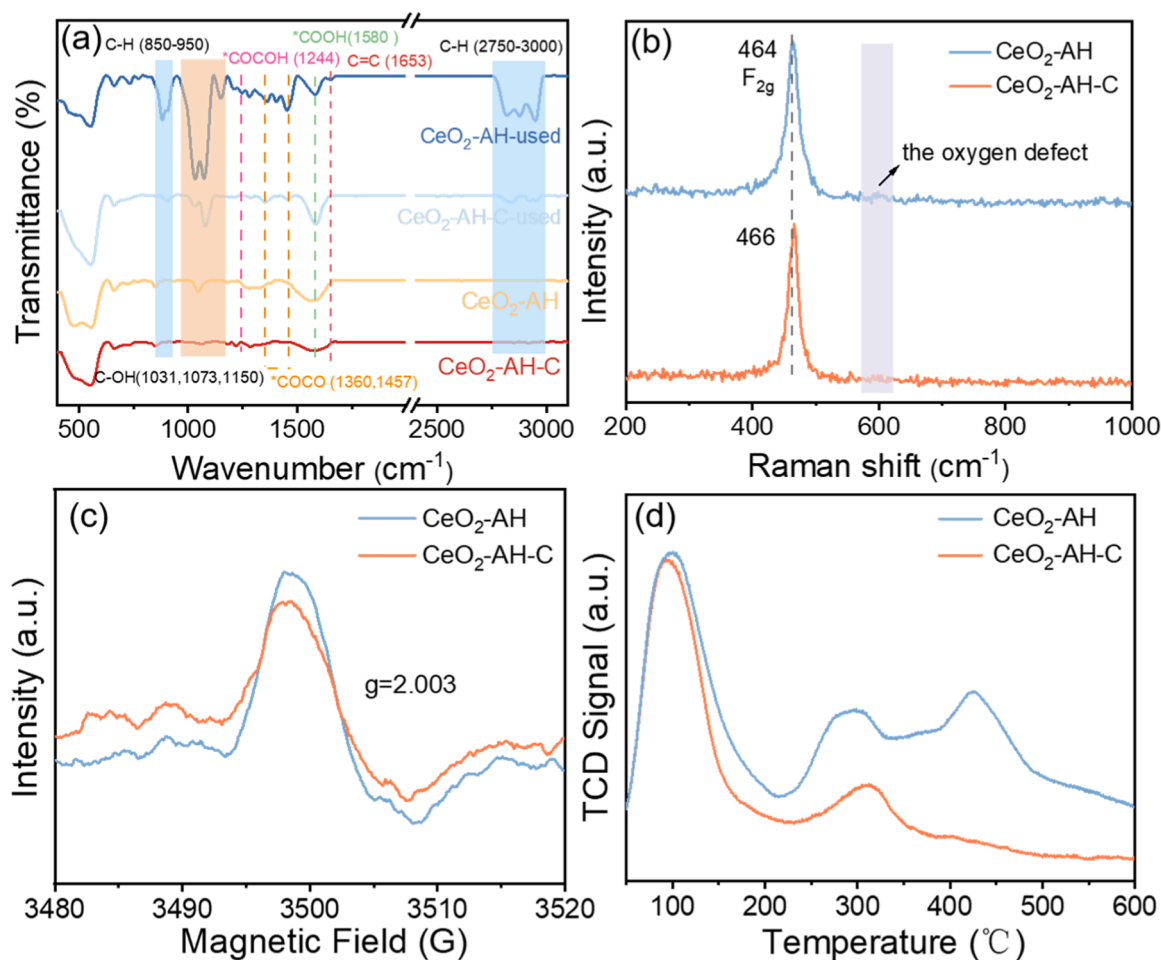


Fig. 3. (a) FTIR spectra of $\text{CeO}_2\text{-AH}$ and $\text{CeO}_2\text{-AH-C}$ before and after the reaction. (b) Raman spectra of $\text{CeO}_2\text{-AH}$ and $\text{CeO}_2\text{-AH-C}$. (c) EPR spectra of $\text{CeO}_2\text{-AH}$ and $\text{CeO}_2\text{-AH-C}$ at room temperature. (d) CO_2 -TPD profiles of $\text{CeO}_2\text{-AH}$ and $\text{CeO}_2\text{-AH-C}$.

of CeO₂-AH, especially that the Ce-N bond at 397.18 eV almost disappears in the CeO₂-AH-C. The calculated N atomic contents are 2.14% and 1.46% for CeO₂-AH and CeO₂-AH-C, respectively. Moreover, compared with the CeO₂-AH-C, the N 1s binding energy of the CeO₂-AH is positive shifted 0.3 eV, indicating that electrons from N species may be transferred to Ce species, which is prone to increase the electron density around Ce atoms and further reduce Ce⁴⁺ to Ce³⁺ in the CeO₂-AH. The overall XPS survey spectra of CeO₂-AH and CeO₂-AH-C were also provided in Fig. S2 and the total atomic contents were summarized in Table S2. Interestingly, the atomic ratios of Ce and O are 1:3.25 and 1:2.97 for CeO₂-AH and CeO₂-AH-C, respectively, which are higher than the standard atomic ratio in CeO₂, indicating that the surface of the CeO₂-AH possesses abundant oxygen-containing groups (e.g. -OH). The surface of CeO₂-AH is enriched with oxygen vacancy, N-doping and Ce-OH structures, which can act as the defect sites to induce the formation of amorphous shell, named N-doped CeO_{2-x}(OH)_y [43].

The above results demonstrates that NH₃·H₂O acts as a base source, can provide abundant unsaturated Ce³⁺ sites and -OH groups as well as N-doping for finely engineering the surface of the CeO₂-AH. The presence of the Ce-OH can act as the Lewis base, and the adjacent coordinately unsaturated Ce³⁺ species near the oxygen vacancy act as the Lewis acid, forming frustrated Lewis acid-base pairs (FLPs). Moreover, the N-doping can induce the reduction of Ce⁴⁺ to Ce³⁺, further increasing the Lewis acidity.

The surface chemical structure can be further revealed by the Fourier Transform infrared spectroscopy (FTIR) and Raman spectra. Fig. 3a and Fig. S3 shows the FTIR spectra of CeO₂-AH and CeO₂-AH-C as well as the two catalysts after the photocatalytic reaction. As indicated in Fig. S3, the bands at around 557, 661, 848, 1049 and 1460–1660 cm⁻¹ of CeO₂-AH correspond mainly to the characteristic peaks of the Ce-O(H) [44–46]. The presence of the Ce-N is corroborated by the presence of Ce-N stretching vibration mode at 480 cm⁻¹ [47]. By comparing the FTIR spectra of the two catalysts before and after the reaction, it can be seen that many new peaks appear after photocatalytic reaction. The peaks at 1031, 1073, 1150 cm⁻¹ indicate the formation of C-OH [33,48]. The narrowed peaks at 1580 cm⁻¹ corresponds to the stretching vibration of *COOH [8,49] which is the important intermediate for CO₂ reduction. In addition, many key intermediates for C₂ products, i.e. *COCO (at 1360 and 1457 cm⁻¹) and *COCO₂H (at 1244 cm⁻¹), are exist in the CeO₂-AH [10]. Moreover, the peak at 1653 cm⁻¹ ascribed to stretching of C=C bond exists only in CeO₂-AH after the reaction [50]. The absorption peaks at 850–950 cm⁻¹ and 2750–3000 cm⁻¹ increase markedly in the CeO₂-AH after reaction, which corresponding to the bending vibration and stretching vibration of C-H bond in vinyl C=CH₂ groups, respectively [9,51]. These results indicate that a lot of CO₂ and CO₂ intermediates are absorbed on the surface of CeO₂-AH during the photocatalytic reaction, especially for the C₂ intermediates. However, all of the peak intensities of the above mentioned bands are dramatically decreased in the CeO₂-AH-C before and after reaction. It confirms that high temperature calcination can largely reduce the content of FLPs and N-doping in the CeO₂-AH-C, which can severely suppress the absorption and activation of CO₂ and its intermediates, especially for the C₂ intermediates.

Raman spectra were also used to demonstrate the changes of their surface properties. As shown in Fig. 3b, the intense band at 464 cm⁻¹ is corresponding to the symmetrical stretching F_{2g} mode of Ce-O, and the weak band at 600 cm⁻¹ is associated with oxygen vacancy [52–54]. The almost disappeared peak at 600 cm⁻¹ in the CeO₂-AH-C reveals a decrease of the surface oxygen vacancy density after thermal treatment. Moreover, the peak of Ce-O bond in CeO₂-AH shifts towards to lower wavenumber compared to that in CeO₂-AH-C, which is resulted from the chemical bond length change, further demonstrating the successful N-doping and the formation of Ce-N bonds in the CeO₂-AH [55,56]. Furthermore, electron paramagnetic resonance (EPR) spectra were employed to analyze the formation of oxygen vacancy. As shown in

Fig. 3c, both samples display an EPR signal at g = 2.003, which can be recognized as oxygen vacancy [57,58]. Obviously, the CeO₂-AH exhibits slightly stronger EPR signal than the CeO₂-AH-C, and the specific oxygen vacancy concentrations calculated according to the EPR spectra are summarized in Table S3, showing that more oxygen vacancies exist in the CeO₂-AH. The CeO₂-AH with high concentration of oxygen vacancies deliver a high possibility to create abundant surface Ce³⁺ Lewis acidic sites, which are in accordance with the XPS results.

The surface reaction involved in the reactant adsorption is vital for photocatalysis, and thus the CO₂ adsorption capability of the catalysts was investigated by CO₂ temperature-programmed desorption (TPD) (CO₂-TPD) characterization (Fig. 3d) and the corresponding data were listed in Table S4. The CO₂-TPD profile of the CeO₂-AH exhibits three major peaks, which can be divided into several CO₂ adsorbed species, i.e. molecule-adsorbed CO₂ (50–180 °C), HCO₃⁻ or carboxylate (180–370 °C), bidentate and polydentate carbonates (b-CO₃²⁻ and p-CO₃²⁻, 370–550 °C) [59,60]. The HCO₃⁻ or carboxylate species at medium temperature came from the reaction of CO₂ with the surface hydroxyl group, and the b-CO₃²⁻ and p-CO₃²⁻ species at high temperature are generated from the strong interaction of CO₂ with oxygen or metal atoms on the catalysts [60,61]. Nevertheless, the high temperature adsorbed CO₂ species are absence in the CeO₂-AH-C, which only shows two peaks at low and medium temperature. Moreover, the surface adsorption quantity of CO₂ is higher on CeO₂-AH (0.66 mmol g⁻¹) than that of CeO₂-AH-C (0.47 mmol g⁻¹). It further demonstrates the importance of the abundant surface FLPs sites and N-doping on CeO₂-AH, which can make an enhanced interaction with CO₂ and thus facilitate for subsequent photocatalytic reduction of CO₂ to high-value hydrocarbons, especially for the C₂ products.

3.2. Evaluation of the optical properties

To investigate the optical properties of the CeO₂-AH and CeO₂-AH-C catalysts, ultraviolet-visible (UV-Vis) diffuse reflectance spectra were conducted. The color of CeO₂-AH (pale yellow) and CeO₂-AH-C (light pale yellow) is presented in the inset of Fig. 4a. As shown in Fig. 4a, the CeO₂-AH exhibits a slightly red shift in the absorption edge in comparison to the CeO₂-AH-C, showing a slightly stronger absorption in the UV and visible light range of the CeO₂-AH. The direct bandgap energies (E_g) are obtained by the Tauc plots, wherein the CeO₂-AH (3.00 eV) displays a narrowed bandgap than that of the CeO₂-AH-C (3.12 eV) (Fig. 4b). It derives from the presence of N-doping can tailor the electronic structure of the CeO₂-AH through generating vacant states above the Fermi level, which could narrow the bandgap and broaden the light absorption edge [5,62,63]. The XPS-valence band spectra show that the valence band potential (E_{VB, XPS}) of CeO₂-AH and CeO₂-AH-C are 1.77 and 1.91 eV, respectively (Fig. 4c). The E_{VB} versus the normal hydrogen electrode (E_{VB, NHE}) of the CeO₂-AH and CeO₂-AH-C can be calculated to be 1.71 and 1.85 eV, respectively, according to the following formula: E_{VB, NHE} = φ + E_{VB, XPS} - 4.44, where φ is the work function of the instrument (4.38 eV) [64]. Then, the conduction band potential (E_{CB}) of the CeO₂-AH and CeO₂-AH-C are calculated to be -1.29 and -1.27 eV, respectively (E_{CB} = E_{VB} - E_g). The energy band diagram is represented in Fig. 4d, confirming that both of the CeO₂-AH and CeO₂-AH-C possess suitable bandgap positions for photocatalytic CO₂ reduction.

The photoluminescence (PL) spectroscopy and time-resolved fluorescence decay spectra were conducted to investigate the charge transfer and the photogenerated electron-hole recombination efficiency. In Fig. 4e, the CeO₂-AH and CeO₂-AH-C display similar emission peaks at about 420 and 600 nm, which are originated from the excitonic recombination from the defects (Ce³⁺ and oxygen vacancies) in the samples with electronic energy levels below the 4 f band [65–67]. Obviously, the intensity of the emission peak decreased significantly in the CeO₂-AH, demonstrating the lower recombination rate of electron-hole in the CeO₂-AH. Time-resolved fluorescence decay spectra and the fitted parameters are displayed in Fig. 4f. The fluorescence

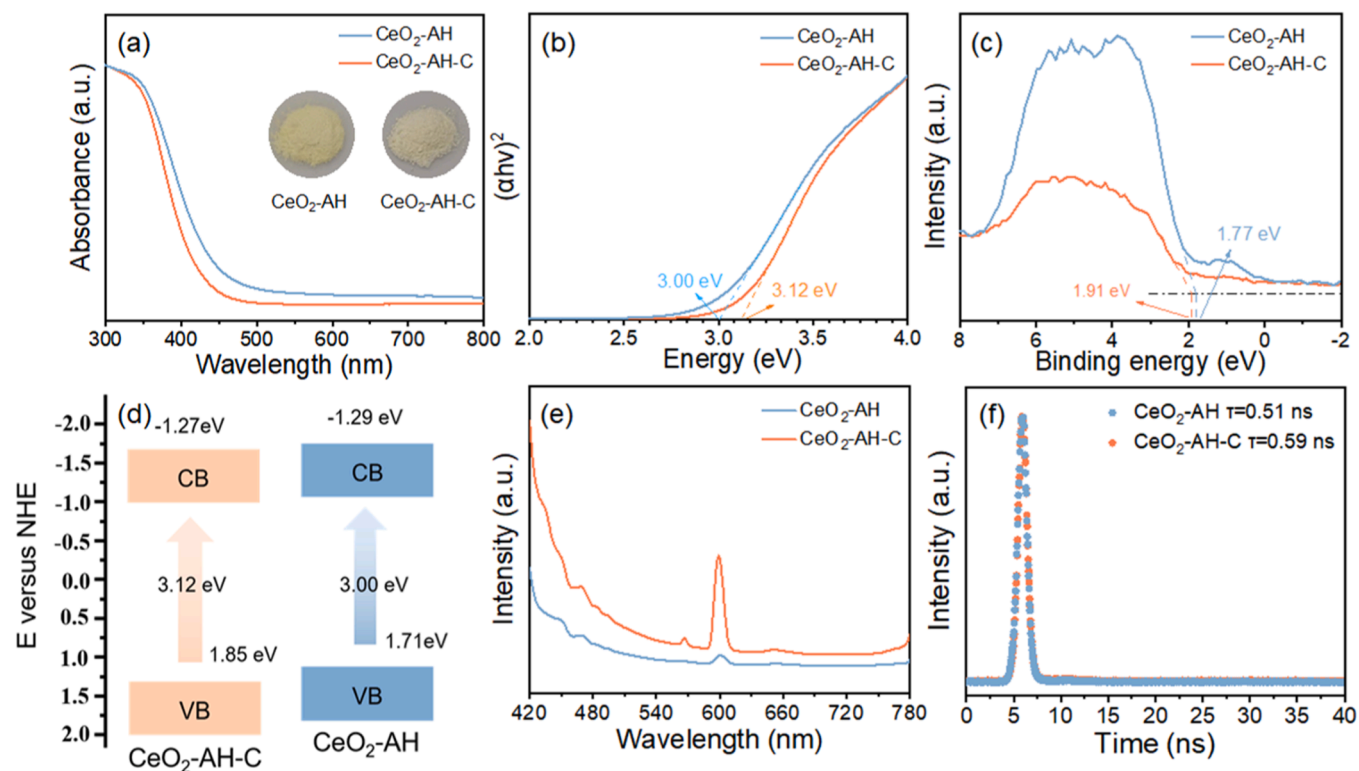


Fig. 4. (a) UV-vis DRS spectra and powder color (inset) of CeO₂-AH and CeO₂-AH-C. (b) Tauc plots of CeO₂-AH and CeO₂-AH-C. (c) VB-XPS spectra of CeO₂-AH and CeO₂-AH-C. (d) Schematic illustrating the electronic band structures (arrows represent the electron transition process; CB, conduction band; VB, valence band). (e) PL spectra and (f) Nanosecond level time-resolved fluorescence decay spectra of CeO₂-AH and CeO₂-AH-C.

lifetime of CeO₂-AH ($\tau = 0.51$ ns) is shorter than that of CeO₂-AH-C ($\tau = 0.59$ ns), indicating faster charge transfer rate in the CeO₂-AH than that of CeO₂-AH-C [68].

3.3. Evaluation of the photocatalytic CO₂ reduction performance

The photocatalytic CO₂ reduction experiments were carried out in the presence of sacrificial agent triethanolamine (TEOA) aqueous solution under light irradiation (see the details in experimental section). Herein, the TEOA act as sacrificial reagents, effectively consuming holes and preventing the recombination of photoinduced electrons and holes on the catalyst surface [69]. Control experiments were firstly performed to study the role of CO₂, photocatalysts, light and TEOA (Fig. S4). No hydrocarbon products are generated in the absence of CO₂ (under Ar atmosphere), confirming that CO₂ is the carbon source in the reaction. When the experiments are conducted in the condition without catalyst, light and TEOA, traces amount of CO and CH₄ are produced, demonstrating that these factors are essential for photocatalytic CO₂ reduction. The traces amount of CO and CH₄ might be resulted from the degradation of TEOA. It should be noted that in order to exclude the degradation effect of TEOA, the CO₂ reduction products of the CeO₂-AH and CeO₂-AH-C were subtracted by the products from the no-catalyst system. As shown in Fig. 5a, for the CeO₂-AH catalyst, the major product is CO ($2\text{e}^- + 2\text{H}^+$, yield = $224.56\text{ }\mu\text{mol g}^{-1}\text{ h}^{-1}$, selectivity (χ) = 28.10%), and is accompanied by CH₄ ($8\text{e}^- + 8\text{H}^+$, yield = $35.35\text{ }\mu\text{mol g}^{-1}\text{ h}^{-1}$, χ = 17.69%) and C₂ hydrocarbons in a remarkable selectivity: C₂H₄ ($12\text{e}^- + 12\text{H}^+$, yield = $33.18\text{ }\mu\text{mol g}^{-1}\text{ h}^{-1}$, χ = 24.91%), and C₂H₂ ($10\text{e}^- + 10\text{H}^+$, yield = $25.84\text{ }\mu\text{mol g}^{-1}\text{ h}^{-1}$, χ = 16.16%). Noted that a small quantity of H₂ ($2\text{e}^- + 2\text{H}^+$, yield = $105\text{ }\mu\text{mol g}^{-1}\text{ h}^{-1}$, χ = 13.14%) is also generated as a competitive reaction and none of liquid products are detected by ¹H NMR. In contrast, the CeO₂-AH-C catalyst (Fig. 5a-II) only leads to relatively low C₁ products, i.e. CO (yield = $55.19\text{ }\mu\text{mol g}^{-1}\text{ h}^{-1}$, χ = 19.63%) and CH₄ (yield = $46.50\text{ }\mu\text{mol g}^{-1}\text{ h}^{-1}$, χ = 66.15%), and

a small amount of H₂ (yield = $40.01\text{ }\mu\text{mol g}^{-1}\text{ h}^{-1}$, χ = 14.22%). In addition, using ¹³CO₂ as the reactive gas, the isotope labeling experiments were conducted to confirm the veracity of the products from CO₂. The results clearly demonstrate that the products including CO, CH₄, C₂H₄ and C₂H₂ are well derived from photocatalytic ¹³CO₂ reduction (Fig. S5).

In order to verify the necessity of the existence of surface FLPs of the CeO₂-AH, the photocatalytic CO₂ reduction reactions were also performed in the presence of molecular Lewis base pyridine or Lewis acid pyrrole. The pyridine or pyrrole can be able to adsorb on and block the Lewis acid or basic sites, respectively, thus are generally used to confirm the presence of the surface FLPs [31]. As indicated in Fig. 5a-III and IV, the addition of either Lewis base pyridine or Lewis acid pyrrole severely decreases the photocatalytic CO₂ reduction performance of the CeO₂-AH, generating a small amount of CO and CH₄, which is even lower than that of the CeO₂-AH-C. The above photocatalytic results reveal that the well-designed surface FLPs and N-doping on the CeO₂-AH are mainly responsible for the enhanced photocatalytic activity and selectivity, especially that the FLPs play the decisive factor. Table S5 summarizes the comparison of photocatalytic CO₂ reduction performance of the CeO₂-AH and state-of-the-art CeO₂-based photocatalysts reported in recent years. Overall, the CeO₂-AH with superior yield and selectivity for hydrocarbon products is comparable to or outperform other CeO₂-based photocatalysts, especially for the C₂ products. The photocatalytic stability of the CeO₂-AH catalyst was evaluated by cycle activity test, wherein the catalyst was collected after the reaction and tested in the cycle. As shown in Fig. 5b, the photocatalytic performance decreased slightly after four cycles, indicating good stability of the CeO₂-AH and the main reason for the slight decrease in performance might be resulted from the structural evolution and the loss of samples during recycling [10]. The stability of the CeO₂-AH catalyst was further analyzed by a series of characterizations, including SEM, XRD and XPS analysis (Fig. S6-S8). The SEM image (Fig. S6) displays that the CeO₂-AH

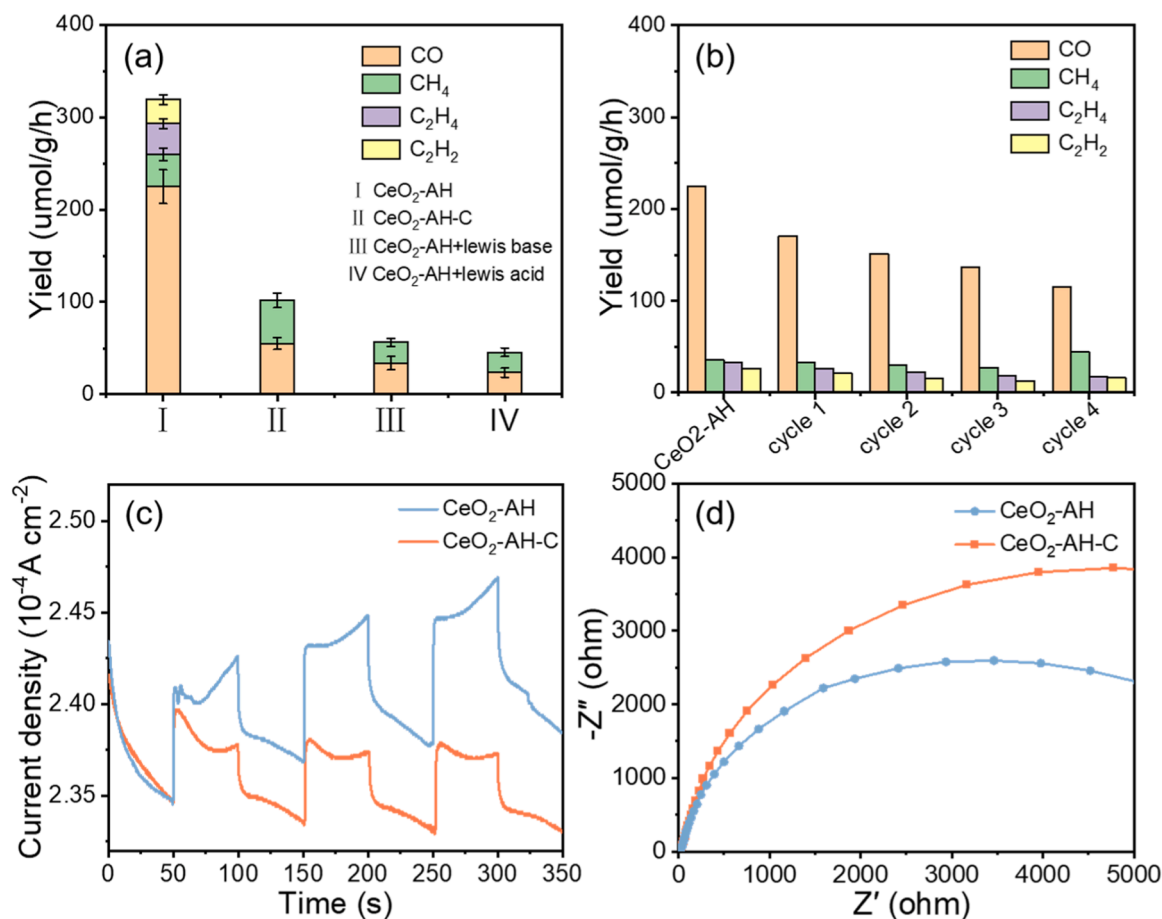


Fig. 5. (a) Photocatalytic CO₂ reduction products yield of I: CeO₂-AH, II: CeO₂-AH-C, III: CeO₂-AH + lewis base (pyridine), IV: CeO₂-AH + lewis acid (pyrrole). (b) Cycle activity test of the photocatalytic CO₂ reduction process over CeO₂-AH. (c) Photocurrent response under light irradiation and (d) EIS Nyquist plots of CeO₂-AH and CeO₂-AH-C.

still maintains the morphology of nanoparticles after photocatalytic reaction. XRD patterns of CeO₂-AH and CeO₂-AH-C before and after catalysis are similar (Fig. S7), further indicating the good stability of the CeO₂-AH catalyst. According to the XPS spectra shown in Fig. S8, the characteristic peaks are well maintained after catalysis, demonstrating there are no significant chemical structure changes. It can be observed that the XPS peaks of the sample after reaction shift towards lower binding energy compared with that pristine one, which might be resulted from the chemisorbed CO₂ intermediates and has been confirmed by the FTIR results. To further demonstrate the effect of charge separation efficiency on the photocatalytic activity of the catalysts, photocurrent-time curves in cyclic dark and light intervals and electrochemical impedance spectroscopy (EIS) Nyquist plots were measured. As shown in Fig. 5c and d, the CeO₂-AH shows a higher photocurrent density and smaller arc radius than that of CeO₂-AH-C, indicating good light utilization and fast charge transfer efficiency in the CeO₂-AH [70], which is consistent with the above UV and PL results.

3.4. Possible mechanisms for the photocatalytic CO₂ reduction reactions

Based on the abovementioned results, we propose the following mechanism for the photocatalytic CO₂ reduction reactions on the CeO₂-AH catalyst (Fig. 6). Upon light irradiation (with photon energy matches or exceeds the bandgap of the catalyst), electrons and holes are generated over the catalysts. The N-doping produces a vacant states above the Fermi level, which can reduce the bandgap of the CeO₂-AH, thus promoting photon absorption and electron-hole separation [5]. The holes react with the TEOA sacrificial electron donor to reduce the rapid

recombination of photogenerated electron-hole pairs [71]. Meanwhile, the photoexcited electrons transfer to the conduction band and participate in reducing the CO₂ adsorbed on the catalyst to varied products including CO, CH₄, C₂H₄ and C₂H₂ (Fig. 6a). The schematic structure of the CeO₂-AH catalyst is shown in Fig. 6b. The Ce-OH groups act as the Lewis base sites, and the adjacent reduced Ce³⁺ sites nearby the oxygen vacancy act as the Lewis acidic sites, constructing the surface FLPs. The abundant surface FLPs on the CeO₂-AH catalyst can effectively bond and active CO₂ molecules (as shown in right side of Fig. 6b), i.e. the C atom in CO₂ gains electrons from surface Lewis base center Ce-OH and form *CO₂ species (* = adsorbed sites), and the lone pair electrons of O atoms in CO₂ can be donated to surface Lewis acid center Ce³⁺ nearby the oxygen vacancy. The adsorbed CO₂ underwent proton coupled electron transfer into CO₂ intermediates such as *COOH and *CO. The synergistic activation effect of the FLPs further prompts the C-C coupling between the two adjacent *CO before desorption, and enable the production of C₂ species through multiple proton coupled electron transfer process [72, 73]. Moreover, the N-doping structure results in electron localization and asymmetric charge distribution, which can be also conducive to *CO dimerization and play a positive role in the photocatalytic reduction of CO₂ to C₂ products [74–76]. It is likely that it is unfavorable for the binding of *H on the active sites of the CeO₂-AH catalyst, limiting the formation of H₂.

Fig. 6c shows the proposed reaction pathways to the formation of CO, CH₄, C₂H₄ and C₂H₂ via proton-coupled two-, eight-, twelve-, and ten-electron steps, respectively (see the following reactions).



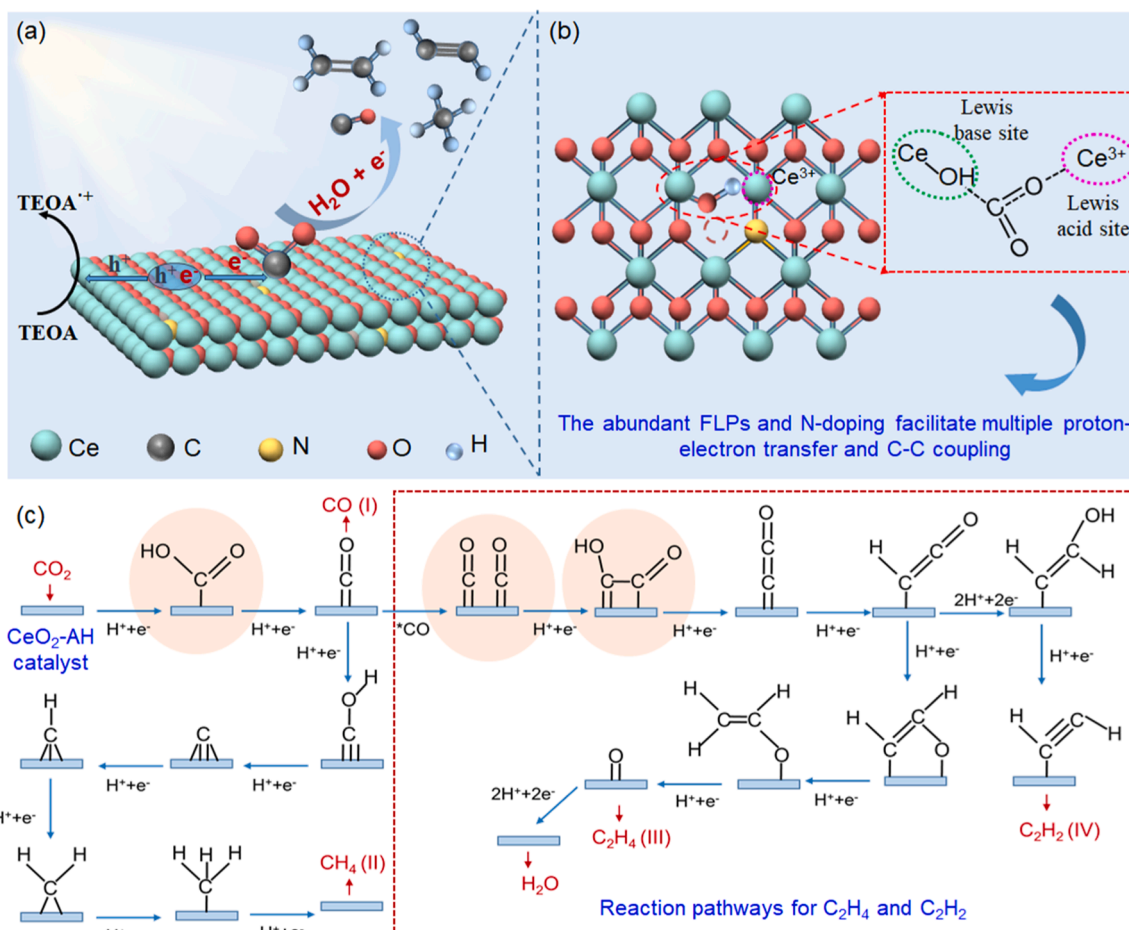
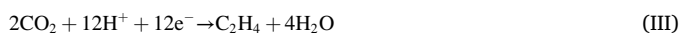


Fig. 6. (a, b) The schematic of CeO₂-AH for photocatalytic CO₂ reduction. (c) The proposed reaction pathways to the formation of CO, CH₄, C₂H₄ and C₂H₂ on CeO₂-AH.



For the CO₂ reduction reaction, the CO₂ get one electron to form *CO₂ intermediate, which mainly acts as an initial reaction step. Then water provides proton to form *COOH, which has been observed in the FTIR spectra (Fig. 3a). The *COOH intermediates accept one proton and electron to produce *CO, which can be desorbed and produce CO (Fig. 6c-I). Herein, the cooperative role of abundant surface FLPs and N-doping could provide more electrons and accessible active sites to capture and stabilize the *CO intermediates, leading to efficient production of high-value hydrocarbons. Therefore, the *CO can be further reduced to CH₄ and C₂ products through multiple proton-electron transfer processes. For the formation of CH₄, the *CO is protonated to form *COH and then dehydroxylated to produce *C, which can be further protonated to *CH→*CH₂→*CH₃→CH₄ (Fig. 6c-II) [77]. In the pathway of C₂H₄ and C₂H₂ (indicated by red rectangle in Fig. 6c), C-C coupling between *CO might be the potential limiting step, and then hydrogenation of the O atoms in *COCO produces *COCO₂H, which is consistent with the observation of *COCO and *COCO₂H in the FTIR spectra. The subsequent multiple proton-electron transfers lead to *CCO→*CHCO. The next proton-electron transfer is important because in it the pathway to C₂H₂ splits from that to C₂H₄. The C₂H₄ pathway proceeds with a protonation of the C atom in the carbonyl group and both C and O are bonded to the surface of the catalyst (*CHCHO) [78]. The following

proton-electron transfer reactions produce *CH₂CHO→C₂H₄ (Fig. 6 c-III). The leaved *O adsorbate is hydrogenated to H₂O finally. In the case of C₂H₂, multiple proton-electron transfer reactions of *CHCO produce *CHCHOH→*CHCH→C₂H₂ (Fig. 6c-IV). Herein, the synergistic effect of surface FLPs and N-doping promote the light absorption, CO₂ bonding and activation, multiple proton-electron transfer processes and C-C coupling reactions, thereby improving the productivity and selectivity of photoreduction of CO₂ to CO, CH₄, C₂H₄ and C₂H₂. In the CeO₂-AH-C catalyst, the high temperature treatment significantly reduces the contents of FLPs and Ce-N/O-Ce-N, which only produce low quantity of C₁ products (i.e. CO and CH₄).

To confirm the above speculated reduction path, we performed density-functional theory (DFT) simulations to investigate the nature of FLPs and N-doping on the CeO₂-AH. Bader charge analysis shows that the surface sites involve atomic local charges of + 1.98 and − 1.38 e for Lewis acid site Ce³⁺ and Lewis base site Ce-OH, respectively (Fig. 7a). The large charge difference results in the formation of active FLPs, which generates a strong electric field on the surface and promotes the polarization and activation of CO₂ molecules. The Lewis acid-base site Ce³⁺—Ce-OH shows a distance of 2.46 Å, which falls in the domain of solid FLPs to activate small molecules such as CO₂ [31]. It has been reported that the FLPs with short acid-base distance are more efficient in capturing and activating of CO₂ molecules due to the strong orbital interactions [58]. Notably, the absence of N-doped CeO₂ FLPs exhibit smaller charge differences (+1.75 and −1.31 e) and larger distances (2.66 Å) (Fig. S9), further suggesting that N-doping increase the Lewis acidity and catalytic activity of the FLPs. Moreover, we analyzed the

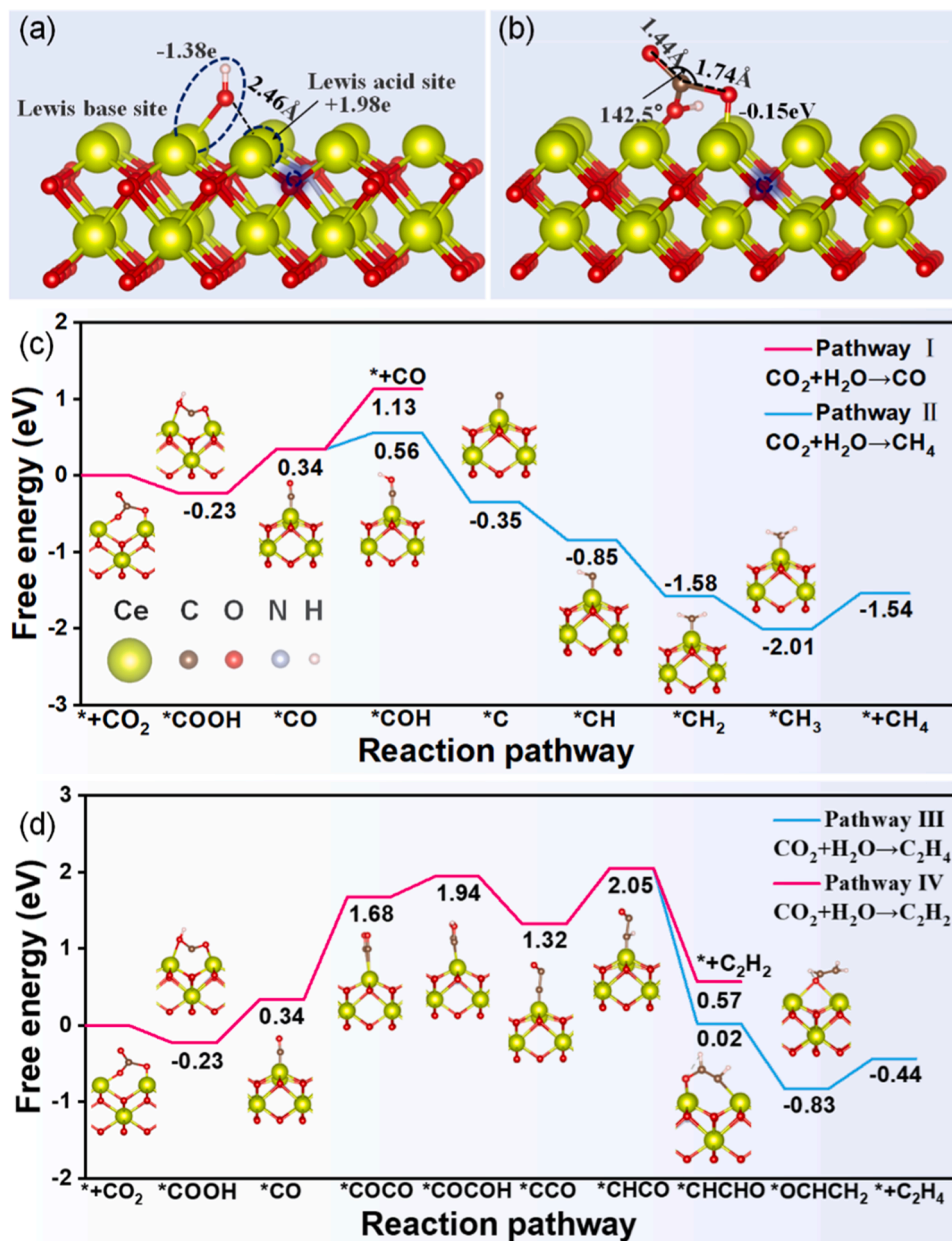


Fig. 7. (a) The configuration of constructing FLPs and N-doping on CeO₂-AH. (b) Adsorption and activation of CO₂ on the FLPs of CeO₂-AH. (c, d) The Gibbs free energy change (ΔG) and reaction pathways for photocatalytic CO₂ reduction to carbon products over CeO₂-AH.

adsorption energy of CO₂ on the surface. The Lewis base sites readily interact with the C atoms of CO₂, and the Ce³⁺ atoms will gain electrons from one of the O atoms of CO₂ (Fig. 7b). The calculated CO₂ adsorption energy is -0.15 eV, demonstrating that the CO₂ adsorption process on the surface of CeO₂-AH is exothermic. In addition, when the CO₂ molecules are adsorbed on the FLPs of CeO₂-AH, the bond lengths of the C=O bond are extended from 1.16 Å to 1.74 Å and 1.44 Å, respectively, and the bond angle of the O=C=O bond is distinctly bent from 180° to 142.5°, revealing that the FLPs can capture and activate the CO₂ efficiently. The Gibbs free energy of *H on the surface is first calculated and the high adsorption energy (0.25 eV) shows that the hydrogen evolution reaction is unfavorable (Fig. S10). Additionally, the Gibbs free energy of CO₂ to key intermediates and products as well as the reaction pathway and the optimized structures of key intermediates on active sites were also calculated. As shown in Fig. 7c, the absorbed CO₂ on the FLPs of CeO₂-AH is activated and hydrogenated to produce *COOH

spontaneously thanks to the preferred bonding with the FLPs, which is subsequently converted to *CO. In the following reaction, the energy required for the conversion of *CO to *COH is 0.56 eV, which is lower than that required for the conversion of *CO to CO (1.13 eV), indicating that the catalytic reaction pathway can also be further proceeded to produce CH₄ besides the great amount of CO products. The reaction paths for the generation of C₂H₄ and C₂H₂ are shown in Fig. 7d. It is worth pointing out that the rate-limiting steps for producing C₂H₄ and C₂H₂ are the formation of key intermediates *COCO and *COCOHO, which have been verified by the FTIR results (Fig. 3a). Moreover, the overall energy values in the reaction paths demonstrate that the photocatalytic reduction of CO₂ to C₂H₄ and C₂H₂ is thermodynamically feasible and the generation of C₂H₄ is much easier than that of C₂H₂, which is corresponding to the experimental results.

4. Conclusion

In summary, we have designed nanostructured CeO₂ photocatalysts through finely engineering the surface properties of CeO₂ with the assistance of NH₃·H₂O, where N-doping and surface FLPs constructed by Lewis acidic coordinately unsaturated Ce³⁺ species and the adjacent Lewis basic Ce-OH groups have been successfully achieved. As demonstrated by the experimental results, the high concentration of surface FLPs and N-doping on the CeO₂-AH promote the light absorption, CO₂ bonding and activation, multiple proton-electron transfer processes and C-C coupling reactions, which are critical to improve its capability for photocatalytic reduction of CO₂ with high productivity and selectivity for C₁ (CO, CH₄) and C₂ (C₂H₄, C₂H₂) hydrocarbon products. This work demonstrates that the synergistic effect of surface FLPs and N-doping could modulate the activity and selectivity of CO₂ photoreduction, showing an effective strategy for developing highly efficient photocatalysts for industrial applications.

CRedit authorship contribution statement

Xiaoli Zheng and Qun Xu established the research line and supervised the work. Xinying Yan performed the experiments and prepared the manuscript. Bo Gao was in charge of the DFT calculation and data analysis. Minjie Cheng and Weiqian Kong took part in discussions and data analysis. Nan Zhou carried out the FTIR measurement. Xueqi Liu participated in ¹³CO₂ isotope labeling experiments. Lina Du and Fei Yuan were responsible for the determination of EPR. Jing Wang, Xiaomin Cui and Gaixiang Zhang directed the experiment. All authors discussed the results.

Declaration of Competing Interest

The authors declare that they have no known competing financial interests or personal relationships that could have appeared to influence the work reported in this paper.

Data Availability

Data will be made available on request.

Acknowledgements

We are grateful to the National Natural Science Foundation of China (No. 21703207, U2004208 and 21773216), and the China Postdoctoral Science Foundation (No. 2018T110738 and 2017M622363), and the Henan Postdoctoral Research Foundation (No. 001702056).

Appendix A. Supporting information

Supplementary data associated with this article can be found in the online version at [doi:10.1016/j.apcatb.2023.123484](https://doi.org/10.1016/j.apcatb.2023.123484).

References

- [1] X. Li, Y. Sun, J. Xu, Y. Shao, J. Wu, X. Xu, Y. Pan, H. Ju, J. Zhu, Y. Xie, Selective visible-light-driven photocatalytic CO₂ reduction to CH₄ mediated by atomically thin CuInS₂ layers, *Nat. Energy* 4 (2019) 690–699, <https://doi.org/10.1038/s41560-019-0431-1>.
- [2] Y. Li, B. Li, D. Zhang, L. Cheng, Q. Xiang, Crystalline carbon nitride supported copper single atoms for photocatalytic CO₂ reduction with nearly 100% CO selectivity, *ACS Nano* 14 (2020) 10552–10561, <https://doi.org/10.1021/acsnano.0c04544>.
- [3] Y. Zhao, Y. Wei, X. Wu, H. Zheng, Z. Zhao, J. Liu, J. Li, Graphene-wrapped Pt/TiO₂ photocatalysts with enhanced photogenerated charges separation and reactant adsorption for high selective photoreduction of CO₂ to CH₄, *Appl. Catal. B Environ.* 226 (2018) 360–372, <https://doi.org/10.1016/j.apcatb.2017.12.071>.
- [4] Q. Zhang, P. Yang, H. Zhang, J. Zhao, H. Shi, Y. Huang, H. Yang, Oxygen vacancies in Co₃O₄ promote CO₂ photoreduction, *Appl. Catal. B Environ.* 300 (2022), 120729, <https://doi.org/10.1016/j.apcatb.2021.120729>.
- [5] Y. Yang, Y.-X. Pan, X. Tu, C.-J. Liu, Nitrogen doping of indium oxide for enhanced photocatalytic reduction of CO₂ to methanol, *Nano Energy* 101 (2022), 107613, <https://doi.org/10.1016/j.nanoen.2022.107613>.
- [6] Y. Huang, K. Wang, T. Guo, J. Li, X. Wu, G. Zhang, Construction of 2D/2D Bi₂Se₃/g-C₃N₄ nanocomposite with High interfacial charge separation and photo-heat conversion efficiency for selective photocatalytic CO₂ reduction, *Appl. Catal. B Environ.* 277 (2020), 119232, <https://doi.org/10.1016/j.apcatb.2020.119232>.
- [7] J. Alberio, Y. Peng, H. García, Photocatalytic CO₂ reduction to C₂+ products, *ACS Catal.* 10 (2020) 5734–5749, <https://doi.org/10.1021/acscatal.0c00478>.
- [8] H. Xu, Z. Wang, H. Liao, D. Li, J. Shen, J. Long, W. Dai, X. Wang, Z. Zhang, Proximity of defects and Ti-H on hydrogenated SrTiO₃ mediated photocatalytic reduction of CO₂ to C₂H₂, *Appl. Catal. B Environ.* 336 (2023), 122935, <https://doi.org/10.1016/j.apcatb.2023.122935>.
- [9] T. Wang, L. Chen, C. Chen, M. Huang, Y. Huang, S. Liu, B. Li, Engineering catalytic interfaces in Cu⁺/CeO₂-TiO₂ photocatalysts for synergistically boosting CO₂ reduction to ethylene, *ACS Nano* 16 (2022) 2306–2318, <https://doi.org/10.1021/acsnano.1c08505>.
- [10] J. Ji, R. Li, H. Zhang, Y. Duan, Q. Liu, H. Wang, Z. Shen, Highly selective photocatalytic reduction of CO₂ to ethane over Au-O-Ce sites at micro-interface, *Appl. Catal. B Environ.* 321 (2023), 122020, <https://doi.org/10.1016/j.apcatb.2022.122020>.
- [11] M. Arumugam, M. Tahir, P. Praserttham, Effect of nonmetals (B, O, P, and S) doped with porous g-C₃N₄ for improved electron transfer towards photocatalytic CO₂ reduction with water into CH₄, *Chemosphere* 286 (2022), 131765, <https://doi.org/10.1016/j.chemosphere.2021.131765>.
- [12] S. Zhu, X. Li, X. Jiao, W. Shao, L. Li, X. Zu, J. Hu, J. Zhu, W. Yan, C. Wang, Y. Sun, Y. Xie, Selective CO₂ photoreduction into C₂ product enabled by charge-polarized metal pair sites, *Nano Lett.* 21 (2021) 2324–2331, <https://doi.org/10.1021/acs.nanolett.1c00383>.
- [13] W. Gao, S. Li, H. He, X. Li, Z. Cheng, Y. Yang, J. Wang, Q. Shen, X. Wang, Y. Xiong, Y. Zhou, Z. Zou, Vacancy-defect modulated pathway of photoreduction of CO₂ on single atomically thin AgInP₂S₆ sheets into olefin gas, *Nat. Commun.* 12 (2021), 4747, <https://doi.org/10.1038/s41467-021-25068-7>.
- [14] D.W. Stephan, Diverse uses of the reaction of frustrated Lewis pair (FLP) with hydrogen, *J. Am. Chem. Soc.* 143 (2021) 20002–20014, <https://doi.org/10.1021/jacs.1c10845>.
- [15] D.W. Stephan, Frustrated Lewis pairs: from concept to catalysis, *Acc. Chem. Res.* 48 (2015) 306–316, <https://doi.org/10.1021/ar500375j>.
- [16] T.A. Rokob, I. Bakó, A. Stirling, A. Hamza, I. Pápai, Reactivity models of hydrogen activation by frustrated Lewis pairs: synergistic electron transfers or polarization by electric field? *J. Am. Chem. Soc.* 135 (2013) 4425–4437, <https://doi.org/10.1021/ja312387q>.
- [17] X. Wang, L. Lu, B. Wang, Z. Xu, Z. Xin, S. Yan, Z. Geng, Z. Zou, Frustrated Lewis pairs accelerating CO₂ reduction on oxyhydroxide photocatalysts with surface lattice hydroxyls as a solid-state proton donor, *Adv. Funct. Mater.* 28 (2018), 1804191, <https://doi.org/10.1002/adfm.201804191>.
- [18] T. Li, W. Zhang, H. Qin, L. Lu, S. Yan, Z. Zou, Inorganic frustrated Lewis pairs in photocatalytic CO₂ reduction, *ChemPhotoChem* 5 (2021) 495–501, <https://doi.org/10.1002/cptc.202000312>.
- [19] J. Sheng, Y. He, M. Huang, C. Yuan, S. Wang, F. Dong, Frustrated Lewis pair sites boosting CO₂ photoreduction on Cs₂CuBr₄ perovskite quantum dots, *ACS Catal.* 12 (2022) 2915–2926, <https://doi.org/10.1021/acscatal.2c00037>.
- [20] L. Du, B. Gao, Q. Tian, X. Zheng, W. Liu, H. Chang, P. Yan, Q. Xu, Frustrated Lewis pairs constructed on 2D amorphous carbon nitride for high-selective photocatalytic CO₂ reduction to CH₄, *Sol. RRL* 5 (2021), 2100673, <https://doi.org/10.1002/solr.202100673>.
- [21] K.K. Ghuman, L.B. Hoch, P. Szymanski, J.Y. Loh, N.P. Kherani, M.A. El-Sayed, G. A. Ozin, C.V. Singh, Photoexcited surface frustrated Lewis pairs for heterogeneous photocatalytic CO₂ reduction, *J. Am. Chem. Soc.* 138 (2016) 1206–1214, <https://doi.org/10.1021/jacs.5b10179>.
- [22] K.K. Ghuman, T.E. Wood, L.B. Hoch, C.A. Mims, G.A. Ozin, C.V. Singh, Illuminating CO₂ reduction on frustrated Lewis pair surfaces: investigating the role of surface hydroxides and oxygen vacancies on nanocrystalline In₂O_{3-x}(OH)_y, *Phys. Chem. Chem. Phys.* 17 (2015) 14623–14635, <https://doi.org/10.1039/c5cp02613j>.
- [23] L.B. Hoch, P. Szymanski, K.K. Ghuman, L. He, K. Liao, Q. Qiao, L.M. Reyes, Y. Zhu, M.A. El-Sayed, C.V. Singh, G.A. Ozin, Carrier dynamics and the role of surface defects: Designing a photocatalyst for gas-phase CO₂ reduction, *Proc. Natl. Acad. Sci. U. S. A.* 113 (2016) E8011–E8020, <https://doi.org/10.1073/pnas.1609374113>.
- [24] L.B. Hoch, T.E. Wood, P.G. O'Brien, K. Liao, L.M. Reyes, C.A. Mims, G.A. Ozin, The rational design of a single-component photocatalyst for gas-phase CO₂ reduction using both uv and visible light, *Adv. Sci.* 1 (2014), 1400013, <https://doi.org/10.1002/advs.201400013>.
- [25] Y. Dong, K.K. Ghuman, R. Popescu, P.N. Duchesne, W. Zhou, J.Y.Y. Loh, A.A. Jelle, J. Jia, D. Wang, X. Mu, C. Kubel, L. Wang, L. He, M. Ghoussoub, Q. Wang, T. E. Wood, L.M. Reyes, P. Zhang, N.P. Kherani, C.V. Singh, G.A. Ozin, Tailoring surface frustrated Lewis pairs of In₂O_{3-x}(OH)_y for gas-phase heterogeneous photocatalytic reduction of CO₂ by isomorphous substitution of In³⁺ with Bi³⁺, *Adv. Sci.* 5 (2018), 1700732, <https://doi.org/10.1002/advs.201700732>.

- [26] T. Yan, N. Li, L. Wang, W. Ran, P.N. Duchesne, L. Wan, N.T. Nguyen, L. Wang, M. Xia, G.A. Ozin, Bismuth atom tailoring of indium oxide surface frustrated Lewis pairs boosts heterogeneous CO₂ photocatalytic hydrogenation, *Nat. Commun.* 11 (2020), 6095, <https://doi.org/10.1038/s41467-020-19997-y>.
- [27] H. Wang, W. Zhang, L. Lu, D. Liu, D. Liu, T. Li, S. Yan, S. Zhao, Z. Zou, Dual-metal hydroxide with ordering frustrated Lewis pairs for photoactivating CO₂ to CO, *Appl. Catal. B Environ.* 283 (2021), 119639, <https://doi.org/10.1016/j.apcatb.2020.119639>.
- [28] D.P.H. Tran, M.-T. Pham, X.-T. Bui, Y.-F. Wang, S.-J. You, CeO₂ as a photocatalytic material for CO₂ conversion: a review, *Sol. Energy* 240 (2022) 443–466, <https://doi.org/10.1016/j.solener.2022.04.051>.
- [29] S. Xie, Z. Wang, F. Cheng, P. Zhang, W. Mai, Y. Tong, Ceria and ceria-based nanostructured materials for photoenergy applications, *Nano Energy* 34 (2017) 313–337, <https://doi.org/10.1016/j.nanoen.2017.02.029>.
- [30] A.K. Sahu, X.S. Zhao, S. Upadhyayula, Ceria-based photocatalysts in water-splitting for hydrogen production and carbon dioxide reduction, *Catal. Rev. Sci. Eng.* (2023) 1–78, <https://doi.org/10.1080/01614940.2023.2166227>.
- [31] S. Zhang, Z.Q. Huang, Y. Ma, W. Gao, J. Li, F. Cao, L. Li, C.R. Chang, Y. Qu, Solid frustrated-Lewis-pair catalysts constructed by regulations on surface defects of porous nanorods of CeO₂, *Nat. Commun.* 8 (2017), 15266, <https://doi.org/10.1038/ncomms15266>.
- [32] S. Zhang, Z. Xia, Y. Zou, F. Cao, Y. Liu, Y. Ma, Y. Qu, Interfacial frustrated Lewis pairs of CeO₂ activate CO₂ for selective tandem transformation of olefins and CO₂ into cyclic carbonates, *J. Am. Chem. Soc.* 141 (2019) 11353–11357, <https://doi.org/10.1021/jacs.9b03217>.
- [33] Z. Wang, J. Zhu, X. Zu, Y. Wu, S. Shang, P. Ling, P. Qiao, C. Liu, J. Hu, Y. Pan, J. Zhu, Y. Sun, Y. Xie, Selective CO₂ photoreduction to CH₄ via Pd⁰-assisted hydrodeoxygenation over CeO₂ nanosheets, *Angew. Chem. Int. Ed.* 61 (2022), e202203249, <https://doi.org/10.1002/anie.202203249>.
- [34] P.K. Prapapati, A. Malik, N. Nandal, S. Pandita, R. Singh, S. Bhandari, S. Saran, S. L. Jain, Morphology controlled Fe and Ni-doped CeO₂ nanorods as an excellent heterojunction photocatalyst for CO₂ reduction, *Appl. Surf. Sci.* 588 (2022), 152912, <https://doi.org/10.1016/j.apsusc.2022.152912>.
- [35] G. Kresse, J. Furthmüller, Efficient iterative schemes for ab initio total-energy calculations using a plane-wave basis set, *Phys. Rev. B* 6 (1996) 15–50, <https://doi.org/10.1103/PhysRevB.54.11169>.
- [36] P.E. Blöchl, Projector augmented-wave method, *Phys. Rev. B* 50 (1994) 17953–17979, <https://doi.org/10.1103/PhysRevB.50.17953>.
- [37] J.P. Perdew, J.A. Chevary, S.H. Vosko, K.A. Jackson, M.R. Pederson, D.J. Singh, C. Fiolhais, Atoms, molecules, solids, and surfaces: Applications of the generalized gradient approximation for exchange and correlation, *Phys. Rev. B* 46 (1992) 6671–6687, <https://doi.org/10.1103/PhysRevB.46.6671>.
- [38] H.J. Monkhorst, J.D. Pack, Special points for Brillouin-zone integrations, *Phys. Rev. B* 13 (1976) 5188–5192, <https://doi.org/10.1103/PhysRevB.13.5188>.
- [39] H. Idriss, On the wrong assignment of the XPS O1s signal at 531–532 eV attributed to oxygen vacancies in photo- and electro-catalysts for water splitting and other materials applications, *Surf. Sci.* 712 (2021), 121894, <https://doi.org/10.1016/j.susc.2021.121894>.
- [40] S.S. Pan, S. Wang, Y.X. Zhang, Y.Y. Luo, F.Y. Kong, S.C. Xu, J.M. Xu, G.H. Li, p-type conduction in nitrogen-doped SnO₂ films grown by thermal processing of tin nitride films, *Appl. Phys. A* 109 (2012) 267–271, <https://doi.org/10.1007/s00339-012-7288-5>.
- [41] Y. Wu, H. Liu, J. Zhang, F. Chen, Enhanced photocatalytic activity of nitrogen-doped titania by deposited with gold, *J. Phys. Chem. C* 113 (2009) 14689–14695, <https://doi.org/10.1021/jp904465d>.
- [42] X. Chen, C. Burda, Photoelectron spectroscopic investigation of nitrogen-doped titania nanoparticles, *J. Phys. Chem. B* 108 (2004) 15446–15449, <https://doi.org/10.1021/jp0469160>.
- [43] L. Wang, Y. Dong, T. Yan, Z. Hu, F.M. Ali, D.M. Meira, P.N. Duchesne, J.Y.Y. Loh, C. Qiu, E.E. Storey, Y. Xu, W. Sun, M. Ghoussoub, N.P. Kherani, A.S. Helmy, G. A. Ozin, Black indium oxide a photothermal CO₂ hydrogenation catalyst, *Nat. Commun.* 11 (2020), 2432, <https://doi.org/10.1038/s41467-020-16336-z>.
- [44] Z. Fang, K.S. Thanthiriatte, D.A. Dixon, L. Andrews, X. Wang, Properties of cerium hydroxides from matrix infrared spectra and electronic structure calculations, *Inorg. Chem.* 55 (2016) 1702–1714, <https://doi.org/10.1021/acs.inorgchem.5b02619>.
- [45] H. Hu, J. Hu, X. Wang, J. Gan, M. Su, W. Ye, W. Zhang, X. Ma, H. Wang, Enhanced reduction and oxidation capability over the CeO₂/g-C₃N₄ hybrid through surface carboxylation: performance and mechanism, *Catal. Sci. Technol.* 10 (2020) 4712–4725, <https://doi.org/10.1039/d0cy00395f>.
- [46] R. Zamir, S.A. Salehizadeh, H.A. Ahangar, M. Shabani, A. Rebelo, J.M.F. Ferreira, Dielectric and optical properties of Ni- and Fe-doped CeO₂ nanoparticles, *Appl. Phys. A* 125 (2019), 393, <https://doi.org/10.1007/s00339-019-2689-3>.
- [47] H. Mohabey, IR spectra, magnetic and thermal studies of copper (II) complex of N-hydroxy-N-(4-chloro) phenyl N'-(4-fluoro) phenyl benzamidine hydrochloride, *Mater. Sci. Res. India* 11 (2014) 63–65, <https://doi.org/10.13005/msri/110108>.
- [48] S. Bai, H. Qiu, M. Song, G. He, F. Wang, Y. Liu, L. Guo, Porous fixed-bed photoreactor for boosting C–C coupling in photocatalytic CO₂ reduction, *eScience* 2 (2022) 428–437, <https://doi.org/10.1016/j.esci.2022.06.006>.
- [49] H. Huang, J. Zhao, B. Weng, F. Lai, M. Zhang, J. Hofkens, M.B.J. Roelfaers, J. A. Steele, J. Long, Site-sensitive selective CO₂ photoreduction to CO over gold nanoparticles, *Angew. Chem. Int. Ed.* 61 (2022), e202204563, <https://doi.org/10.1002/anie.202204563>.
- [50] Y. Bi, M. Ma, Z. Liao, Z. Tong, Y. Chen, R. Wang, Y. Ma, G. Wu, One-dimensional Ni@Co/C@PPy composites for superior electromagnetic wave absorption, *J. Colloid Interface Sci.* 605 (2022) 483–492, <https://doi.org/10.1016/j.jcis.2021.07.050>.
- [51] W. Xie, K. Li, X.H. Liu, X. Zhang, H. Huang, P-mediated Cu–N₄ sites in carbon nitride realizing CO₂ photoreduction to C₂H₄ with selectivity modulation, *Adv. Mater.* 35 (2023), e2208132, <https://doi.org/10.1002/adma.202208132>.
- [52] Y. Wang, F. Wang, Q. Song, Q. Xin, S. Xu, J. Xu, Heterogeneous ceria catalyst with water-tolerant Lewis acidic sites for one-pot synthesis of 1,3-diols via prins condensation and hydrolysis reactions, *J. Am. Chem. Soc.* 135 (2013) 1506–1515, <https://doi.org/10.1021/ja310498c>.
- [53] C. Zhu, X. Wei, W. Li, Y. Pu, J. Sun, K. Tang, H. Wan, C. Ge, W. Zou, L. Dong, Crystal-plane effects of CeO₂(110) and CeO₂(100) on photocatalytic CO₂ reduction: synergistic interactions of oxygen defects and hydroxyl groups, *ACS Sustain. Chem. Eng.* 8 (2020) 14397–14406, <https://doi.org/10.1021/acssuschemeng.0c04205>.
- [54] Z. Shen, Q. Xia, Y. Li, C. Yin, Z. Ge, X. Li, Y. Wang, Adsorption-enhanced nitrogen-doped mesoporous CeO₂ as an efficient visible-light-driven catalyst for CO₂ photoreduction, *J. CO₂ Util.* 39 (2020), 101176, <https://doi.org/10.1016/j.jcou.2020.101176>.
- [55] Y. Gao, P. Yin, Effect of bond dispersion on raman spectra shift in II–VI semiconductor nanocrystals, *Inorg. Chem.* 58 (2019) 4859–4868, <https://doi.org/10.1021/acs.inorgchem.8b03359>.
- [56] X. Yang, Z. Dong, C.Q. Sun, Effects of doping concentration on bond length and bond energy studied by Raman shift, *Appl. Phys. Lett.* 123 (2023), 053101, <https://doi.org/10.1063/5.0160714>.
- [57] H. Jiang, L. Wang, H. Kaneko, R. Gu, G. Su, L. Li, J. Zhang, H. Song, F. Zhu, A. Yamaguchi, J. Xu, F. Liu, M. Miyauchi, W. Ding, M. Zhong, Light-driven CO₂ methanation over Au-grafted Ce_{0.95}Ru_{0.05}O₂ solid-solution catalysts with activities approaching the thermodynamic limit, *Nat. Catal.* 6 (2023) 519–530, <https://doi.org/10.1038/s41929-023-00970-z>.
- [58] W. Zhang, Z. Yang, H. Wang, L. Lu, D. Liu, T. Li, S. Yan, H. Qin, T. Yu, Z. Zou, Crystal facet-dependent frustrated Lewis pairs on dual-metal hydroxide for photocatalytic CO₂ reduction, *Appl. Catal. B Environ.* 300 (2022), 120748, <https://doi.org/10.1016/j.apcatb.2021.120748>.
- [59] K. Yoshikawa, H. Sato, M. Kaneeda, J.N. Kondo, Synthesis and analysis of CO₂ adsorbents based on cerium oxide, *J. CO₂ Util.* 8 (2014) 34–38, <https://doi.org/10.1016/j.jcou.2014.10.001>.
- [60] W. Li, L. Jin, F. Gao, H. Wan, Y. Pu, X. Wei, C. Chen, W. Zou, C. Zhu, L. Dong, Advantageous roles of phosphate decorated octahedral CeO₂{111}/g-C₃N₄ in boosting photocatalytic CO₂ reduction: charge transfer bridge and Lewis basic site, *Appl. Catal. B Environ.* 294 (2021), 120257, <https://doi.org/10.1016/j.apcatb.2021.120257>.
- [61] Y. Pu, Y. Luo, X. Wei, J. Sun, L. Li, W. Zou, L. Dong, Synergistic effects of Cu₂O-decorated CeO₂ on photocatalytic CO₂ reduction: Surface Lewis acid/base and oxygen defect, *Appl. Catal. B Environ.* 254 (2019) 580–586, <https://doi.org/10.1016/j.apcatb.2019.04.093>.
- [62] W. Yu, J. Zhang, T. Peng, New insight into the enhanced photocatalytic activity of N-, C- and S-doped ZnO photocatalysts, *Appl. Catal. B Environ.* 181 (2016) 220–227, <https://doi.org/10.1016/j.apcatb.2015.07.031>.
- [63] W. Fu, J. Fan, Q. Xiang, Ag₂S quantum dotsdecorated on porous cubic-CdS nanosheetsassembled flowers for photocatalytic CO₂ reduction, *Chin. J. Chem.* 41 (2022) 2206039–2206047, <https://doi.org/10.14102/j.cnki.0254-5861.2022-0090>.
- [64] X. Li, B. Kang, F. Dong, Z. Zhang, X. Luo, L. Han, J. Huang, Z. Feng, Z. Chen, J. Xu, B. Peng, Z.L. Wang, Enhanced photocatalytic degradation and H₂/H₂O₂ production performance of S-pCN/WO_{2.72} S-scheme heterojunction with appropriate surface oxygen vacancies, *Nano Energy* 81 (2021), 105671, <https://doi.org/10.1016/j.nanoen.2020.105671>.
- [65] T.N. Ravishanker, T. Ramakrishnapa, G. Nagaraju, H. Rajanaika, Synthesis and characterization of CeO₂ nanoparticles via solution combustion method for photocatalytic and antibacterial activity studies, *Chemistryopen* 4 (2015) 146–154, <https://doi.org/10.1002/open.201402046>.
- [66] S. Phoka, P. Laokul, E. Swatsitang, V. Promarak, S. Seraphin, S. Maensiri, Synthesis, structural and optical properties of CeO₂ nanoparticles synthesized by a simple polyvinyl pyrrolidone (PVP) solution route, *Mater. Chem. Phys.* 115 (2009) 423–428, <https://doi.org/10.1016/j.matchemphys.2008.12.031>.
- [67] A. Hezam, K. Namratha, Q.A. Drmosh, D. Ponnammma, J. Wang, S. Prasad, M. Ahmed, C. Cheng, K. Byrappa, CeO₂ nanostructures enriched with oxygen vacancies for photocatalytic CO₂ reduction, *ACS Appl. Nano Mater.* 3 (2020) 138–148, <https://doi.org/10.1021/acsnanm.9b01833>.
- [68] Q. Chen, X. Chen, M. Fang, J. Chen, Y. Li, Z. Xie, Q. Kuang, L. Zheng, Photo-induced Au–Pd alloying at TiO₂{101} facets enables robust CO₂ photocatalytic reduction into hydrocarbon fuels, *J. Mater. Chem. A* 7 (2019) 1334–1340, <https://doi.org/10.1039/c8ta09412h>.
- [69] S. Han, B. Li, L. Huang, H. Xi, Z. Ding, J. Long, Construction of ZnIn₂S₄-CdIn₂S₄ microspheres for efficient photo-catalytic reduction of CO₂ with visible light, *Chin. J. Chem.* 41 (2022) 2201007–2201013, <https://doi.org/10.14102/j.cnki.0254-5861.2021-0026>.
- [70] S. Zhu, N. Li, D. Zhang, T. Yan, Metal/oxide heterostructures derived from Prussian blue analogues for efficient photocatalytic CO₂ hydrogenation to hydrocarbons, *J. CO₂ Util.* 64 (2022), 102177, <https://doi.org/10.1016/j.jcou.2022.102177>.

- [71] K. Niu, Y. Xu, H. Wang, R. Ye, H.L. Xin, F. Lin, C. Tian, Y. Lum, K.C. Bustillo, M. M. Doeff, M.T.M. Koper, J. Ager, R. Xu, H. Zheng, A spongy nickel-organic CO₂ reduction photocatalyst for nearly 100% selective CO production, *Sci. Adv.* 3 (2017), e1700921, <https://doi.org/10.1126/sciadv.1700921>.
- [72] W. Li, Y. Zhang, Y. Wang, W. Ran, Q. Guan, W. Yi, L. Zhang, D. Zhang, N. Li, T. Yan, Graphdiyne facilitates photocatalytic CO₂ hydrogenation into C₂₊ hydrocarbons, *Appl. Catal. B Environ.* 340 (2024), 123267, <https://doi.org/10.1016/j.apcatb.2023.123267>.
- [73] K. Yan, D. Wu, T. Wang, C. Chen, S. Liu, Y. Hu, C. Gao, H. Chen, B. Li, Highly selective ethylene production from solar-driven CO₂ reduction on the Bi₂S₃@In₂S₃ catalyst with In-S_V-Bi active sites, *ACS Catal.* 13 (2023) 2302–2312, <https://doi.org/10.1021/acscatal.2c05741>.
- [74] Y. Zhou, F. Che, M. Liu, C. Zou, Z. Liang, P. De Luna, H. Yuan, J. Li, Z. Wang, H. Xie, H. Li, P. Chen, E. Bladt, R. Quintero-Bermudez, T.-K. Sham, S. Bals, J. Hofkens, D. Sinton, G. Chen, E.H. Sargent, Dopant-induced electron localization drives CO₂ reduction to C₂ hydrocarbons, *Nat. Chem.* 10 (2018) 974–980, <https://doi.org/10.1038/s41557-018-0092-x>.
- [75] P. Song, B. Hu, D. Zhao, J. Fu, X. Su, W. Feng, K. Yu, S. Liu, J. Zhang, C. Chen, Modulating the asymmetric atomic interface of copper single atoms for efficient CO₂ electroreduction, *ACS Nano* 17 (2023) 4619–4628, <https://doi.org/10.1021/acsnano.2c10701>.
- [76] P. Chen, P. Zhang, X. Kang, L. Zheng, G. Mo, R. Wu, J. Tai, B. Han, Efficient electrocatalytic reduction of CO₂ to ethane over nitrogen-doped Fe₂O₃, *J. Am. Chem. Soc.* 144 (2022) 14769–14777, <https://doi.org/10.1021/jacs.2c05373>.
- [77] J. Zhao, Z. Chen, J. Zhao, Metal-free graphdiyne doped with sp-hybridized boron and nitrogen atoms at acetylenic sites for high-efficiency electroreduction of CO₂ to CH₄ and C₂H₄, *J. Mater. Chem. A* 7 (2019) 4026–4035, <https://doi.org/10.1039/c8ta11825f>.
- [78] F. Calle-Vallejo, M.T.M. Koper, Theoretical considerations on the electroreduction of CO to C₂ species on Cu(100) electrodes, *Angew. Chem. Int. Ed.* 52 (2013) 7282–7285, <https://doi.org/10.1002/anie.201301470>.